PHYSICAL REVIEW MATERIALS **8**, 054006 (2024)

Electrical transport crossover and large magnetoresistance in selenium deficient van der Waals $HfSe_{2-x}$ ($0 \leqslant x \leqslant 0.2$)

Wenhao Liu[1], Yangzi Zheng[1], Aswin Lakshmi Narayanan Kondusamy[1], David L. Scherm[1], Anton V. Malko[1], and Bing Lv[1,2,*]

[1]*Department of Physics, The University of Texas at Dallas, Richardson, Texas 75080, USA*
[2]*Department of Materials Science and Engineering, The University of Texas at Dallas, Richardson, Texas 75080, USA*

(Received 3 September 2023; accepted 14 May 2024; published 29 May 2024)

Transition-metal dichalcogenides (TMDs) have received much attention in the past decade not only due to the new fundamental physics, but also due to the emergent applications in these materials. Currently chalcogenide deficiencies in TMDs are commonly believed either during the high-temperature growth procedure or in the nanofabrication process resulting in significant changes of their reported physical properties in the literature. Here, we perform a systematic study involving pristine stochiometric $HfSe_2$, Se-deficient $HfSe_{1.9}$, and $HfSe_{1.8}$. Stochiometric $HfSe_2$ transport results show semiconducting behavior with a gap of 1.1eV. Annealing $HfSe_2$ under high vacuum at room temperature causes the Se loss resulting in $HfSe_{1.9}$, which shows unconventionally large magnetoresistivity following the extended Kohler rule at low temperatures below 50 K. Moreover, a clear electrical resistivity crossover, mimicking the metal-insulator transition, is observed in the $HfSe_{1.9}$ single crystal. Further increasing the degree of deficiency in $HfSe_{1.8}$ results in complete metallic electrical transport at all temperatures down to 2 K. Such a drastic difference in the transport behaviors of stoichiometric and Se-deficient $HfSe_2$ further emphasizes the defect control and engineering could be an effective method that could be used to tailor the electronic structure of 2D materials, potentially unlock new states of matter, or even discover new materials.

DOI: 10.1103/PhysRevMaterials.8.054006

I. INTRODUCTION

The large class of layered transition-metal dichalcogenides (TMDs) has emerged as a potential channel material alternative to silicon due to the requirements of ultrathin, high integrability, and low-power electronics for modern electronic systems. Due to their rich crystalline structures, wide variety of constituent elements, and the control offered via external perturbation such as chemical doping, proximity, gating, strain, and moiré patterning, many fascinating electronic and optical properties have been discovered in this family. For instance, strong correlation phenomena such as superconductivity charge-density wave, heavy fermions, and Mott insulators are demonstrated [1–5]. Two-dimensional (2D) magnetism including room-temperature ferromagnetic (FM), spirals, skyrmion-type antiferromagnetic (AFM), and possible quantum spin liquid are shown in TMDs doped with magnetic elements. Topology nontriviality, such as Weyl semimetals, is observed in T_d-WTe_2 [6–8]. In addition, coupling between ferroelectricity and superconductivity has been examined in T_d-WTe_2 and T_d-$MoTe_2$. Moreover, fascinating optical properties including strong photoluminescence and large optical excitation are demonstrated in WSe_2 [9,10]

In spite of this significant progress, many open questions and challenges remain. One major challenge is the difficulty of controlling and predicting the properties of materials with high deficiency or defects. Chalcogenide deficiencies are ubiquitous in TMD materials and can profoundly alter their mechanical, chemical, electrical, optical, and thermal functionality, and their coupling with each other. Previous works showed that defects not only modify the ground-state properties, excited-state properties, and a material's responses to external fields [11,12], but also could lead to new structures, unusual transport behaviors, novel magnetism, and even superconductivity [13–15]. To realize the full potential of the TMD system, understanding and controlling defects and deficiencies is required.

With this motivation, we completed one model study on the Se-deficiency effect in $HfSe_2$. $HfSe_2$ adopts the $1T$ structure which consists of an octahedral prism and shows semiconducting behaviors with a band gap of 1.13 eV^3 [16]. A high on/off current ratio exceeding 7.5×10^6 and high mobility is also demonstrated in $HfSe_2$, attracting considerable interest [17,18]. The 1T-HfS_2 has a ~2-eV band gap, while its sister compounds $1T$-$HfTe_2$ show metallic behaviors with a high magnetoresistance of 3000% [19,20]. The band gap in $HfSe_2$ can be tuned via external pressure or lithium intercalation [21,22], showing high potential for future electronic applications. $HfSe_2$ is not stable in air, and previous work revealed the Hf metals in the surface reacted preferentially with oxygen, leading to the formation of more insulating HfO_2 islands or thin layer [23,24]. In this work, we find the room-temperature storage under vacuum causes significant changes of the Se deficiency, and we further investigate the low-temperature transport behavior of $HfSe_{2-x}$ ($0 \leqslant x \leqslant 0.2$) through carefully controlling the Se deficiency. A clear transition from semiconducting behavior to metallic conductor behavior has

---

[*] Corresponding author: blv@utdallas.edu

been observed with the evolution of the Se deficiency. Moreover, unusually high magnetoresistance is observed in the low-temperature region ($T < 25$ K) for the $HfSe_{1.9}$ sample. This sample also follows the extended Kohler rule in the low temperatures below 50 K.

II. EXPERIMENT DETAILS

Single crystals were synthesized using a two-step process. First, polycrystalline samples were synthesized using Hf pieces (99.8%) and Se shots (99.999%) in appropriate ratios (discussed below). The samples were first heated at 600 °C for 3 days in an evacuated silica tube followed by furnace cooling to get the polycrystalline precursors. In the second step, single crystals were synthesized using the chemical vapor transport (CVT) method. The preformed polycrystalline samples were sealed in evacuated silica tubes with I_2 as the transport agent (1 mg/cm^3). Platelike large single crystals with dimensions of 3 mm×3 mm were obtained with a 2-week reaction time, and source- and growth-zone temperatures fixed at 950 and 850 °C, respectively. To obtain the stoichiometric $HfSe_2$ crystals, 5% extra Se (i.e., Hf:Se = 1:2.1) was needed. $HfSe_{1.8}$ crystals could be obtained through CVT synthesis with a Hf:Se ratio larger than 1:1.7. The optimized condition to obtain $HfSe_{1.8}$ crystals with uniform Se deficiencies was with the ratio of Hf: Se = 1:1.5 with the temperature profile of 950 °C (source) and 850 °C (sink) for 2 weeks.

The control of the $HfSe_2$ and $HfSe_{1.8}$ stoichiometry could be done easily by tuning the Hf and Se ratio in the CVT process; however, the precise control of the Se deficiencies down to 0.1 in the CVT-grown process was rather difficult. These reactions often yielded batches of crystals with nonuniform Se deficiencies. Precise growth control of $HfSe_{1.9}$ single crystals could be obtained through postannealing the as-grown stoichiometric $HfSe_2$ crystals in a silica tube under ultrahigh vacuum at 350 °C for 1–5 days. The best control of $HfSe_{1.9}$ samples could be obtained via annealing $HfSe_2$ at room temperature under high vacuum or in the glovebox with inert atmosphere for 3 months. Careful comparison of the annealed samples with the low-yield as-grown $HfSe_{1.9}$ was done to ensure our sample quality and our observation were intrinsic. This room-temperature annealing effect on $HfSe_2$ also highlighted the essential need for proper storage of the samples.

The exact chemical composition of the crystals obtained was verified by energy-dispersive x-ray spectroscopy (EDX) on a DM07 Zeiss Supra 40 scanning electron microscope. X-ray diffraction was conducted on single-crystal samples using a Rigaku Smart Lab x-ray diffractometer equipped with Cu-$K\alpha$ radiation. Resistivity was conducted on the freshly cleaved surfaces of $HfSe_{2-x}$ using the four-probe method in Quantum Design Physical Property Measurement System down to 1.8 K.

The single-crystal x-ray data were measured on a Bruker SMAER diffractometer with an Apen II area detector with a Mo $K\alpha$ source ($\lambda = 0.710\,73$ Å).

Figure 1 shows the x-ray-diffraction (XRD) patterns of $HfSe_{2-x}$ crystals with different deficiencies. The inset shows the optical image of $HfSe_2$ on a millimeter-scale grid with a freshly cleaved surface used for x-ray diffraction. All $HfSe_{2-x}$ crystallizes in the 1*T* structure. Only the *00l* peaks are shown, demonstrating the crystallographic *c* axis is perpendicular to the flat surface of the single crystal. The left inset shows that upon increasing Se deficiencies, the x-ray peaks shift slightly towards higher angles, indicating the small reduction of the out-of-plane lattice parameter with the increasing Se deficiency. The refined *c*-lattice parameters for $HfSe_2$, $HfSe_{1.9}$, and $HfSe_{1.8}$ were $c = 6.169(2)$, 6.156(7), and 6.139(1) Å, respectively. Notably, there was no additional XRD peak observed beyond the (*00l*) peak with increasing Se deficiency. Furthermore, to rigorously validate the crystal structure, a single-crystal x-ray diffractometer was employed. All specimens from three batches of $HfSe_2$, $HfSe_{1.9}$, and $HfSe_{1.8}$ consistently revealed identical structures, affirming the absence of any secondary phases. The element ratio was confirmed by energy-dispersive EDX in Supplemental Material [25], which revealed the Hf: Se molar ratio was 1:1.97 ± 0.03, 1:1.88 ± 0.01, and 1:1.79 ± 0.03. For convenience, we used $HfSe_2$, $HfSe_{1.9}$, and $HfSe_{1.8}$ to indicate these phases, respectively. Such small standard deviations indicate high homogeneity of the element's distribution, and high quality of our samples.

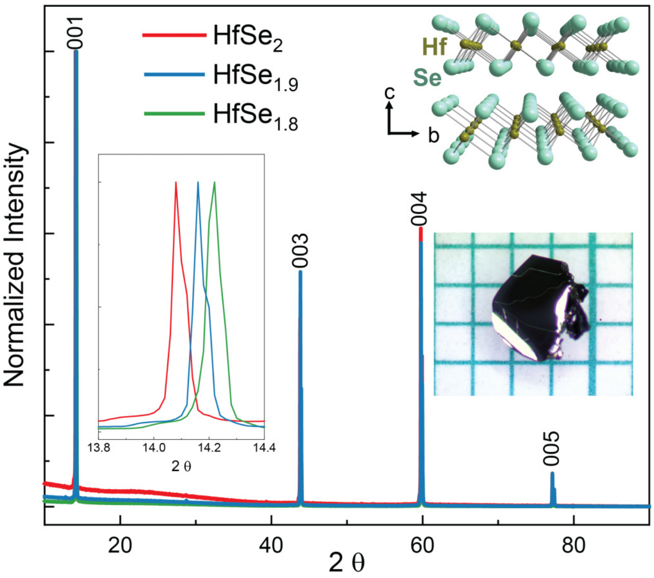

FIG. 1. X-ray-diffraction pattern of $HfSe_{2-x}$ single crystals. Left inset: enlarged view of (*001*) peak of $HfSe_{2-x}$ single crystals. Right top inset: illustration of the crystal structure of $HfSe_{2-x}$. Right bottom inset: optical image of as-grown $HfSe_2$ single crystal.

The temperature-dependent electrical resistivity data for three crystals are shown in Fig. 2. The resistivity of stoichiometric $HfSe_2$, as indicated in Fig. 2(a), increases upon cooling of the temperature, demonstrating typical semiconducting behavior. The sample exceeds the upper resistance limit of our equipment below 200 K. The resistivity can be fit quite well using the thermal activation model $\rho = \rho_0 \exp(E_a/K_B T)$, where ρ_0 is a prefactor and k_B is the Boltzmann constant. Figure 2(a) inset shows the results of linear fitting of $\ln(\rho)$ vs $(1/T)$, where the activation energy is estimated to be ∼330 meV.

Figure 2(b) shows the optical absorption spectra of stoichiometric $HfSe_2$. To properly measure absorption spectrum of $HfSe_2$ crystal, we employed microscope-based

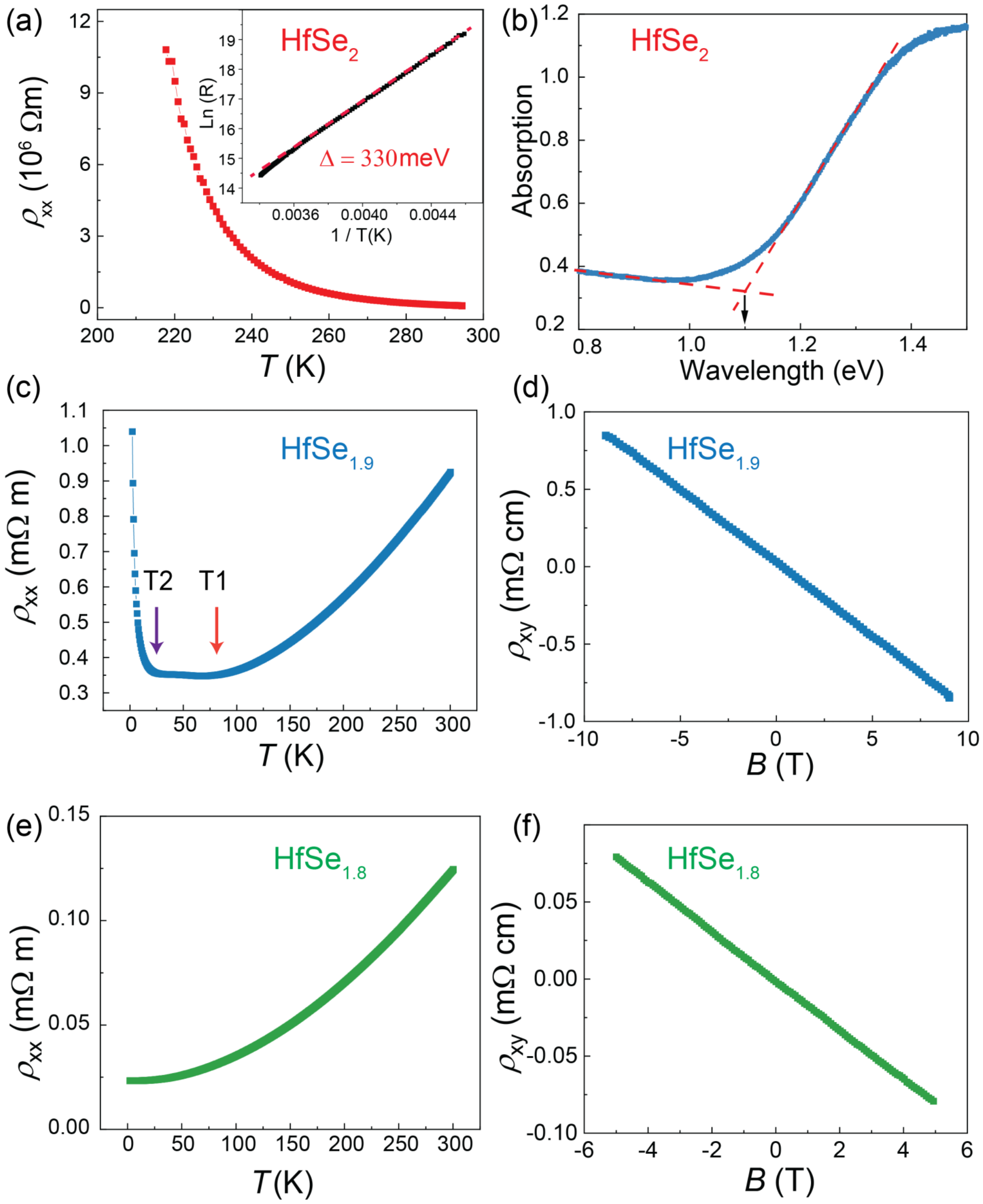

FIG. 2. (a) Temperature dependence of resistivity in stoichiometric $HfSe_2$. Inset: ln (R) vs $1/T$ and the thermal activation gap. Red dashed line: fitting using thermal activation model. (b) Optical absorption spectra of stoichiometric $HfSe_2$. (c), (d) Temperature dependence of resistivity and Hall resistivity of $HfSe_{1.9}$. (e), (f) Temperature dependence of resistivity and Hall resistivity of $HfSe_{1.8}$.

system which can measure optical absorption spectra from micrometer-sized samples. The $HfSe_2$ flake and a reference sample were illuminated by a fiber-coupled white-light source (Thorlabs SLS201L) through a 20× objective lens. The transmission spectra collected by the microscope passed through a monochromator and were recorded by a charge-coupled device camera. By applying the Tauc method, the estimated optical band gap of $HfSe_2$ was found to be about 1.1 eV.

Figure 2(c) shows the temperature dependence of resistivity of $HfSe_{1.9}$ where a clear resistivity crossover is observed. From room temperature of 300 K to temperatures higher than 100 K (indicated by T1), dR/dT was positive, indicating metallic behavior in this range. Between 20 and 100 K, resistivity stayed nearly constant, and started to rise again when the temperature was below 20 K (indicated by T2). The resistivity values at room temperature (0.95 mΩ m) were fairly comparable to that at 2 K (1.05 mΩ m) but were significantly smaller than the room-temperature value (8000 mΩ m) for the $HfSe_2$ sample, suggesting the effect of charge carriers' increase was more dominant than the impurity scattering effects caused by defects. The Hall resistivity of $HfSe_{1.9}$, shown in the inset of Fig. 2(c), exhibited a linear relation with external magnetic fields. The slope was negative, demonstrating charge carriers were mainly electrons and the estimated carrier density from Hall data using single-band model was about $6.6\times10^{18}\,\mathrm{cm}^{-3}$. Further increasing the amount of Se deficiency to produce $HfSe_{1.8}$ led to the complete metallic behavior across the whole temperature range as illustrated in Fig. 2(d). Further

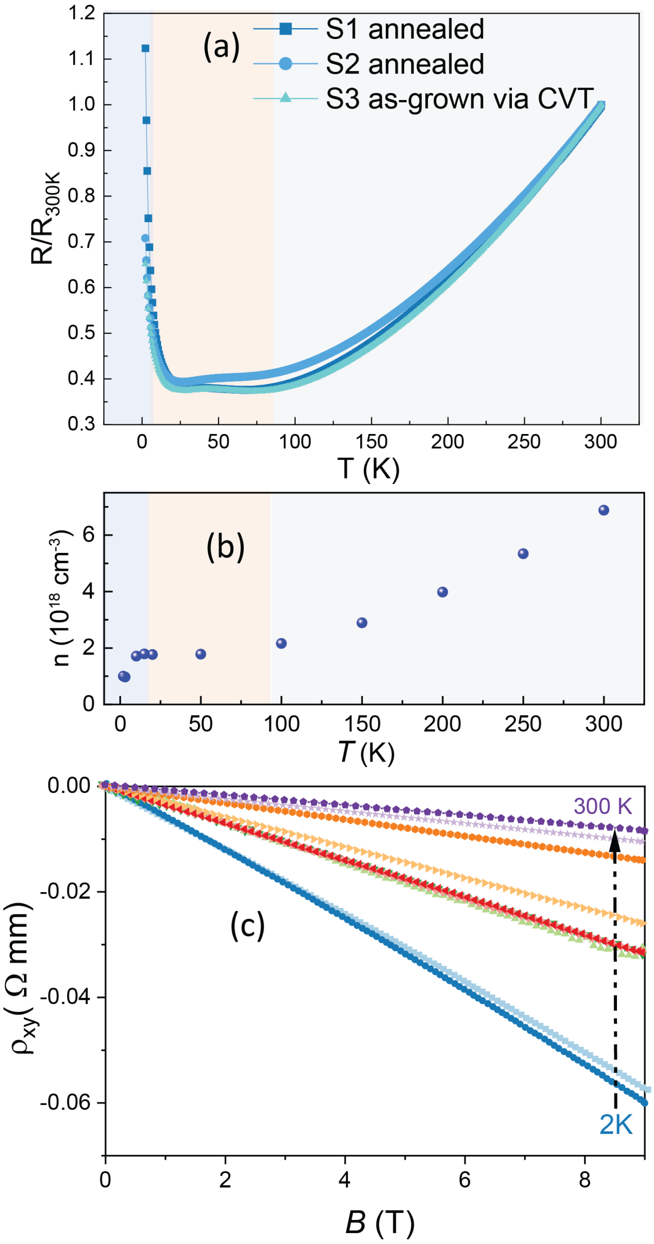

FIG. 3. (a) Temperature dependence of normalized resistance of annealed $HfSe_{1.9}$. S1 and S2 indicate two samples from different batches synthesized via annealing, and S3 indicates low-yielding as-grown $HfSe_{1.9}$ synthesized via CVT. (b) Temperature-dependent carrier concentration of $HfSe_{1.9}$ determined from the Hall resistivity in (c).

Hall-effect measurements suggested the further increase of the electron charge carriers to 3.9×10^{19} cm^{-3}, and accounted for the emergence of complete metallic behavior for $HfSe_{1.8}$ phase.

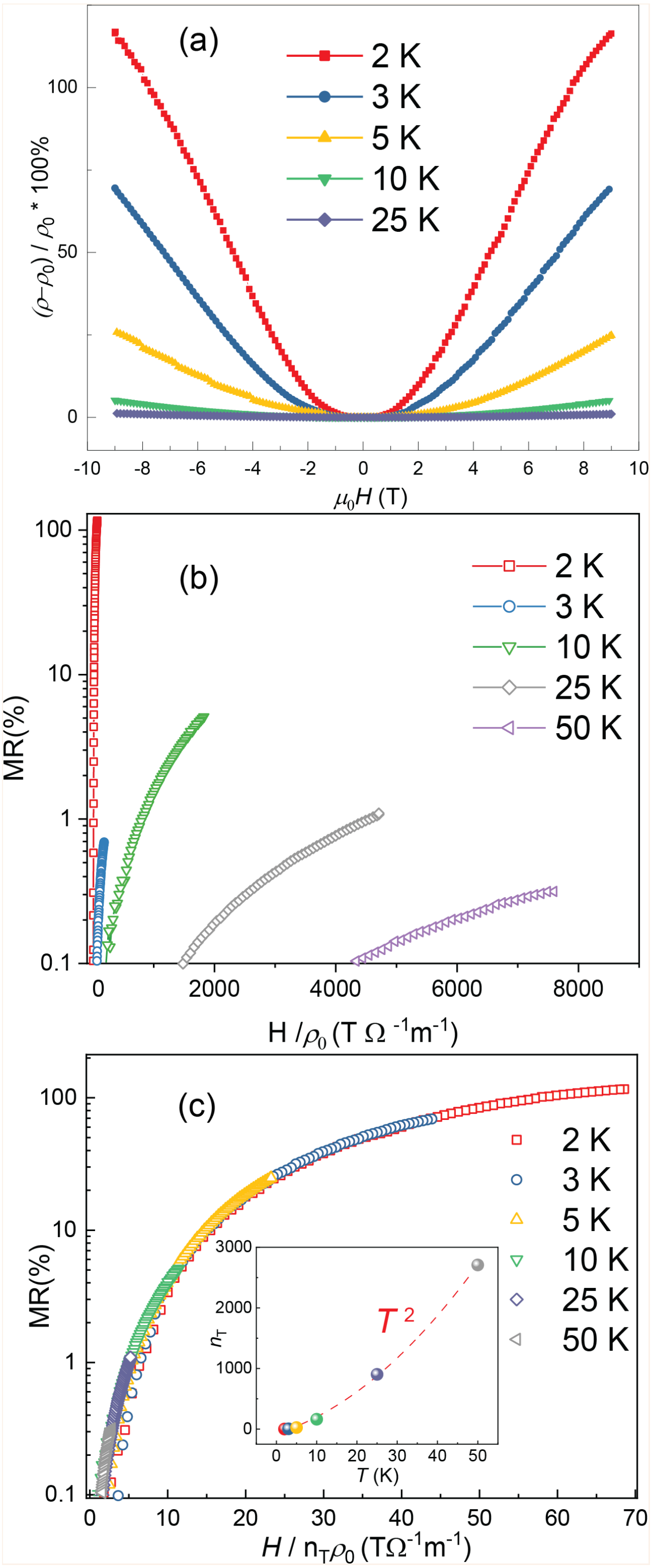

FIG. 4. (a) Magnetoresistance of $HfSe_{1.9}$ up to 9 T at various temperatures. (b) The violation of Kohler's rule for the MR in (a). (c) Test for extended Kohler's scaling of magnetoresistance in $HfSe_{1.9}$ single crystal.

To further understand the metal-insulator-like resistivity crossover in the $HfSe_{1.9}$ sample, low-temperature Hall measurements at various temperatures were carried out on $HfSe_{1.9}$. Overall linear dispersion with negative slopes were measured in the whole temperature range investigated, reinforcing that the carrier density was dominantly electrons near the Fermi surface. A comparison between electrical resistivity and calculated carrier density from Hall data at different temperatures is plotted in Fig. 3. The carrier density decreased monotonically with decreasing of the temperature. This nicely coincided with the corresponding temperature-dependent resistivity results. Upon increasing temperature from 2 to 25 K, $HfSe_{1.9}$ exhibited semiconducting behavior where the resistivity decreased while the carrier density increased. Between 25 and 100 K, both the carrier density and resistivity remained constant, indicating potential equilibrium in this system. At high temperatures above 100 K, $HfSe_{1.9}$ became metal, as indicated by the positive slope of *dR/dT*. The increase in carrier density and the temperature leads in the enhancement of the collisions between carriers and phonons, which may result in the increasement of resistivity in the high-temperature region.

Figure 4(a) shows the magnetoresistance (MR) of $HfSe_{1.9}$ up to 9 T at different temperatures. At 2 K, the MR evolved gradually from a positive curvature to a negative curvature when the external magnetic field was increased above 6 T. This did not follow the common quadratic behavior. Magnetoresistance ratio, which is defined as $MRR = (\rho(B)/\rho_0 - 1)\times 100\%$, could reach 120% at 2 K with an external magnetic field of 9 T. This value was quite high considering the absence of magnetic elements in this material.

Large magnetoresistance is often linked with topologically nontrivial band structure. Prime examples of this are WTe_2 and $MoTe_2$ [26,27]. In Hf-based compounds such as $HfTe_2$, large nonsaturating magnetoresistance has been observed [20,28], which was attributed to carrier compensation as initially $HfTe_2$ was reported to be trivial semimetal with coexisting electrons and holes at the Fermi surface. But, recently some clear Dirac-like cone features at the center of the Brillouin zone were observed from angle-resolved photoemission spectroscopy studies on the high-quality molecular-beam epitaxy-grown $HfTe_2$ monolayer, suggesting materials quality might be crucial for further studies of this system. Disorders, on the other hand, were also proposed to modify the magnetoresistance and yield positive large magnetoresistance in low-dimensional materials [29]. This provided another possibility of the origin of substantial magnetoresistivity observed in Se-deficient $HfSe_{1.9}$ systems.

Our $HfSe_{1.9}$ sample here likely underwent very subtle electronic structure changes compared to the pristine $HfSe_2$ sample. Meanwhile, the more Se-deficient $HfSe_{1.8}$ sample showed the most encountered quadratic behavior with a MRR of about 1% [25], and demonstrated a normal metallic phase in the compounds with more Se deficient.

In semiclassical transport theory, the temperature and magnetic dependence of resistance can often be analyzed via Kohler's rule, which dictatea that the magnetoresistance MR obeys the scaling behavior of $f\ [H/(\rho_0)]$, where $\mathrm{MR} = [\rho(H) - \rho_0]/\rho_0$. Here, H is the magnetic field, with $\rho(H)$ and ρ_0 being the resistivity at H and zero field, respectively. Kohler's rule holds if there is a constant single-carrier type and the scattering time τ is the same on all points on the Fermi surface [26,30], as demonstrated in various metals [31]. The validity of Kohler's rule was extended to several semiconductors and even in cuprate superconductors if the Fermi surface remained largely temperature independent [32–34].

In $HfSe_{1.9}$, MR curves at fixed temperatures vs H/ρ_0 did not collapse into one single curve, which demonstrated the violation of Kohler's rule, as illustrated in Fig. 4(b). The violation of Kohler's rule could be caused by different mechanisms including multiple scattering rates [35–37], multiband effect [38,39], carrier-density change induced by Fermi-surface shift or temperature [40,41], etc., which usually implies the possibility of emergent physics phenomena hidden in this phase.

Recently, several other models have been proposed for the case where Kohler's rule was violated. For example, the extended Kohler's rule $\mathrm{MR} = f[H/(n_T\rho_0)]$ was raised and accounted for the systems with change of total carrier density [42]. Here, n_T was responsible for the carrier change. In $HfSe_{1.9}$, a clear temperature dependence of carrier density could be observed, as shown in Fig. 3(c). The unusual large magnetoresistance collapsed into one single line if n_T was considered in H/ρ_0, following extended Kohler's rule, as shown in Fig. 4(c). Here, we define n_T at 2 K equal to 1 and temperature dependence of n_T is shown in the inset of Fig. 4(c). n_T obtained in our sample followed a rough T^2 scaling, which could be attributed to the thermal-induced change in the carrier density, as could be seen in other systems like TaP [42].

In conclusion, we reported the room-temperature effect on the chemical stoichiometry and carried out systematic research on the impact the defects played on a model system $HfSe_{2-x}$. Stoichiometric $HfSe_2$ showed semiconducting behavior with a band gap of 1.1 eV as determined by the optical absorption spectrum. Se deficiency caused electron doping in the system, which could tune the carrier density and the Fermi level, and changed the system from semiconducting $HfSe_2$ to metallic $HfSe_{1.8}$. In the metastable middle compound $HfSe_{1.9}$, competition between the metallic and insulating phases became more paramount and might account for the large magnetoresistance following the extended Kohler's scaling. The rich phase transitions of $HfSe_{2-x}$ provided another material platform to investigate the mechanism of Kohler and extended Kohler's scaling. Besides, the differences between stoichiometric and room-temperature annealed $HfSe_2$ further demonstrated that the preparation, storage time, and defect (level) should be clarified precisely in the chemical and physical property analysis, especially the device characterization of the TMD family.

ACKNOWLEDGMENTS

This work at The University of Texas at Dallas is supported by U.S. Air Force Office of Scientific Research Grant No. FA9550-19-1–0037, National Science Foundation (NSF) Grant No. DMREF-2324033, and Office of Naval Research (ONR) Grant No. N00014-23-1–2020. We also acknowledge the support from the AOSFR Defense University Research Instrumentation Program (DURIP) Grant No. FA9550-21-1–0297. The work of Y.Z. and A.V.M. has been supported by NSF-ECCS Award No. 2202278.

[1] L. Li, X. Deng, Z. Wang, Y. Liu, M. Abeykoon, E. Dooryhee, A. Tomic, Y. Huang, J. B. Warren, E. S. Bozin, S. J. L. Billinge, Y. Sun, Y. Zhu, G. Kotliar, and C. Petrovic, npj Quantum Mater. **2**, 11 (2017).

[2] S. C. De La Barrera, M. R. Sinko, D. P. Gopalan, N. Sivadas, K. L. Seyler, K. Watanabe, T. Taniguchi, A. W. Tsen, X. Xu, D. Xiao, and B. M. Hunt, Nat. Commun. **9**, 1427 (2018).

[3] H. Wu, S. Li, W. Liu, and B. Lv, Inorg. Chem. **62**, 3525 (2023).

[4] J. Pan, C. Guo, C. Song, X. Lai, H. Li, W. Zhao, H. Zhang, G. Mu, K. Bu, T. Lin, X. Xie, M. Chen, and F. Huang, J. Am. Chem. Soc. **139**, 4623 (2017).

[5] W. Liu, M. R. Osanloo, X. Wang, S. Li, N. Dhale, H. Wu, M. L. Van de Put, S. Tiwari, W. G. Vandenberghe, and B. Lv, Phys. Rev. B **104**, 024507 (2021).

[6] Y. Qi, P. G. Naumov, M. N. Ali, C. R. Rajamathi, W. Schnelle, O. Barkalov, M. Hanfland, S. C. Wu, C. Shekhar, Y. Sun, V. Süß, M. Schmidt, U. Schwarz, E. Pippel, P. Werner, R. Hillebrand, T. Förster, E. Kampert, S. Parkin, R. J. Cava, C. Felser, B. Yan, and S. A. Medvedev, Nat. Commun. **7**, 11038 (2016).

[7] Y. Wang, E. Liu, H. Liu, Y. Pan, L. Zhang, J. Zeng, Y. Fu, M. Wang, K. Xu, Z. Huang, Z. Wang, H. Z. Lu, D. Xing, B. Wang, X. Wan, and F. Miao, Nat. Commun. **7**, 13142 (2016).

[8] M. Sato and Y. Ando, Rep. Prog. Phys. **80**, aa6ac7 (2017).

[9] M. S. Fuhrer and J. Hone, Nat. Nanotechnol. **8**, 146 (2013).

[10] M. R. Islam, N. Kang, U. Bhanu, H. P. Paudel, M. Erementchouk, L. Tetard, M. N. Leuenberger, and S. I. Khondaker, Nanoscale **6**, 10033 (2014).

[11] Q. Liang, Q. Zhang, X. Zhao, M. Liu, and A. T. S. Wee, ACS Nano **15**, 2165 (2021).

[12] Z. Lin, B. R. Carvalho, E. Kahn, R. Lv, R. Rao, H. Terrones, M. A. Pimenta, and M. Terrones, 2D Mater. **3**, 022002 (2006).

[13] W. H. Blades, N. J. Frady, P. M. Litwein, S. J. McDonnell, and P. Reinke, J. Phys. Chem. C **124**, 15337 (2020).

[14] S. Li, Y. Zhang, H. Wu, H. Zhai, W. Liu, D. P. Petit, J. S. Oh, J. Denlinger, G. T. McCandless, J. Y. Chan, R. J. Birgeneau, G. Li, M. Yi, and B. Lv, npj Quantum Mater. **6**, 80 (2021).

[15] W. Liu, S. Li, H. Wu, N. Dhale, P. Koirala, and B. Lv, Phys. Rev. Mater. **5**, 014802 (2021).

[16] D. L. Greenaway and R. Nitsche, J. Phys. Chem. Solids **26**, 1445 (1965).

[17] M. Kang, S. Rathi, I. Lee, D. Lim, J. Wang, L. Li, M. A. Khan, and G. H. Kim, Appl. Phys. Lett. **106**, 143108 (2015).

[18] M. J. Mleczko, C. Zhang, H. R. Lee, H. H. Kuo, B. Magyari-Köpe, R. G. Moore, Z. X. Shen, I. R. Fisher, Y. Nishi, and E. Pop, Sci. Adv. **3**, e1700481 (2017).

[19] Y. Y. Wang, P. J. Guo, S. Xu, K. Liu, and T. L. Xia, Phys. Rev. B **101**, 035145 (2020).

[20] S. Mangelsen, P. G. Naumov, O. I. Barkalov, S. A. Medvedev, W. Schnelle, M. Bobnar, S. Mankovsky, S. Polesya, C. Näther, H. Ebert, and W. Bensch, Phys. Rev. B **96**, 205148 (2017).

[21] X. Zhang, B. Liu, S. Liu, J. Li, R. Liu, P. Wang, Q. Dong, S. Li, H. Tian, Q. Li, and B. Liu, J. Alloys Compd. **867**, 158923 (2021).

[22] C. Julien and E. Hatzikraniotis, J. Phys. Soc. Jpn. **51**, 880 (1982).

[23] G. Mirabelli, C. McGeough, M. Schmidt, E. K. McCarthy, S. Monaghan, I. M. Povey, M. McCarthy, F. Gity, R. Nagle, G. Hughes, A. Cafolla, P. K. Hurley, and R. Duffy, J. Appl. Phys. **120**, 125102 (2016).

[24] Q. Yao, L. Zhang, P. Bampoulis, and H. J. W. Zandvliet, J. Phys. Chem. C **122**, 25498 (2018).

[25] See Supplemental Material at http://link.aps.org/supplemental/10.1103/PhysRevMaterials.8.054006 for EDX and magnetoresistance results.

[26] D. H. Keum, S. Cho, J. H. Kim, D.-H. Choe, H.-J. Sung, M. Kan, H. Kang, J.-Y. Hwang, S. W. Kim, H. Yang, K. J. Chang, and Y. H. Lee, Nat. Phys. **11**, 482 (2015).

[27] M. N. Ali, J. Xiong, S. Flynn, J. Tao, Q. D. Gibson, L. M. Schoop, T. Liang, N. Haldolaarachchige, M. Hirschberger, N. P. Ong, and R. J. Cava, Nature (London) **514**, 205 (2014).

[28] S. Mangelsen and W. Bensch, Inorg. Chem. **59**, 1117 (2020).

[29] G. Kastrinakis, Europhys. Lett. **42**, 345 (1998).

[30] Ross H. McKenzie, J. S. Qualls, S. Y. Han, and J. S. Brooks, Phys. Rev. B **57**, 11854 (1998).

[31] A. B. Pippard, *Magnetoresistance in Metals*, 1st ed. (Cambridge University Press, Cambridge, 1989).

[32] A. Narayanan, M. D. Watson, S. F. Blake, N. Bruyant, L. Drigo, Y. L. Chen, D. Prabhakaran, B. Yan, C. Felser, T. Kong, P. C. Canfield, and A. I. Coldea, Phys. Rev. Lett. **114**, 117201 (2015).

[33] A. Malinowski, V. L. Bezusyy, and P. Nowicki, Phys. Rev. B **95**, 014521 (2017).

[34] M. K. Chan, M. J. Veit, C. J. Dorow, Y. Ge, Y. Li, W. Tabis, Y. Tang, X. Zhao, N. Barišić, and M. Greven, Phys. Rev. Lett. **113**, 177005 (2014).

[35] J. M. Harris, Y. F. Yan, P. Matl, N. P. Ong, P. W. Anderson, T. Kimura, and K. Kitazawa, Phys. Rev. Lett. **75**, 1391 (1995).

[36] S. Rößler, C. Koz, L. Jiao, U. K. Rößler, F. Steglich, U. Schwarz, and S. Wirth, Phys. Rev. B **92**, 060505(R) (2015).

[37] N. Maksimovic, I. M. Hayes, V. Nagarajan, J. G. Analytis, A. E. Koshelev, J. Singleton, Y. Lee, and T. Schenkel, Phys. Rev. X **10**, 041062 (2020).

[38] Y. Sun, T. Taen, T. Yamada, S. Pyon, T. Nishizaki, Z. Shi, and T. Tamegai, Phys. Rev. B **89**, 144512 (2014).

[39] A. Wang, D. Graf, Y. Liu, Q. Du, J. Zheng, H. Lei, and C. Petrovic, Phys. Rev. B **96**, 121107(R) (2017).

[40] P. Cheng, H. Yang, Y. Jia, L. Fang, X. Y. Zhu, G. Mu, and H.-H. Wen, Phys. Rev. B **78**, 134508 (2008).

[41] Y. Wu, N. H. Jo, M. Ochi, L. Huang, D. Mou, S. L. Bud'ko, P. C. Canfield, N. Trivedi, R. Arita, and A. Kaminski, Phys. Rev. Lett. **115**, 166602 (2015).

[42] J. Xu, F. Han, T. T. Wang, L. R. Thoutam, S. E. Pate, M. Li, X. Zhang, Y. L. Wang, R. Fotovat, U. Welp, X. Zhou, W. K. Kwok, D. Y. Chung, M. G. Kanatzidis, and Z. L. Xiao, Phys. Rev. X **11**, 041029 (2021).